Front glass crack inspection of thin-film solar photovoltaic modules using high-order ultrasonic Lamb waves

Dicky Silitonga [a,*], Nico F. Declercq [a], Fodil Meraghni [b], Bertrand Boussert [c]

[a] George W. Woodruff School of Mechanical Engineering, Georgia Institute of Technology, GT-Europe, IRL 2958 Georgia Tech – CNRS, 2 rue Marconi, Metz 57070, France
[b] Arts et Métiers ParisTech, LEM3 UMR CNRS 7239, 4 rue Augustin Fresnel, Metz 57078, France
[c] Electrical and Computer Engineering, Georgia Institute of Technology, GT-Europe, 2 rue Marconi, Metz 57070, France

A B S T R A C T

Ensuring the structural integrity of solar photovoltaic modules is crucial to maintain power production efficiency and fulfill the anticipated product lifespan. Hence, implementing quality control procedures and structural health monitoring is necessary throughout the stages of manufacture and operation. The ultrasonic examination has some benefits compared to electroluminescence and infrared approaches, namely in identifying mechanical flaws in the front glass. The Lamb waves (LW) method is an auspicious inspection approach among ultrasonic-based methods. This is primarily attributed to its quicker measurement speed than the standard ultrasonic c-scan. The LW method offers an advantage in terms of its ability to provide long-range coverage. The predominant approach in LW inquiry often centers on using fundamental modes within the low-frequency range. Nevertheless, the findings of this investigation demonstrate that the higher-order mode exhibits superior effectiveness for the specific objective of this research, as it displays a higher level of sensitivity towards cracks in the front glass of the module. The current study ultimately showcases the use of the LW scan. A damage indication threshold is determined by the fraction of energy spectral density (ESD) associated with the crack-sensitive mode. This technology effectively produces a comprehensive map of the designated area by comparing the ESD values at various measurement positions with a predetermined threshold. This map provides precise indications of the existence of areas that are affected by cracks.

1. Introduction

Solar photovoltaics (PV) have become the major player in the global shift to sustainable energy generation. A growing concern for green development, supported by the endorsements from the authorities towards solar power generation, leads to extensive installations of solar PV modules. Continuous advancement of PV research and development has brought incremental improvement in efficiency and cost per kWh, becoming a crucial factor accelerating the widespread utilization of this versatile green electricity generator. Thin film solar modules have gained attraction due to their unique advantages over traditional crystalline modules. Thin film technology utilizes various materials, such as amorphous silicon, cadmium telluride, and copper indium gallium selenide, to create solar cells with a thickness of several hundred nanometers to a few micrometers [1]. This ultra-thin design offers several benefits, including flexibility, lightweight construction, and the ability to be integrated into various applications [2,3]. Furthermore, thin film modules can be produced using less raw material and energy [4], reducing manufacturing costs and having a lower carbon footprint than silicon wafer-based PV modules [5].

In line with the exponential projected growth of solar PV installations, such systems' quality assurance and performance monitoring have become very important. Quality control and structural health monitoring ensure the system's efficiency, safety, and stability over its expected lifetime [6,7]. To cope with the increasing production and installation, it becomes necessary to have techniques capable of accomplishing the inspection tasks themselves and are time-efficient to keep up with the pace of manufacturing lines.

Electroluminescence (EL) and infrared (IR) thermography are commonly used for inspecting solar panels. EL leverages the process of light emission resulting from the radiative recombination of charge carriers. This mechanism is similar to the phenomenon observed in light-

* Corresponding author.
E-mail address: dsilitonga@gatech.edu (D. Silitonga).

emitting diodes (LEDs). It allows for detecting various defects in solar panels, such as cell cracks and cell malfunctions. IR thermography uses thermal distribution to identify hotspots, cell malfunctions, and areas with temperature anomaly with respect to the normal cells. Those methods are quick but primarily effective on the electric current path only, such as cells and conductors. In addition, environmental conditions, such as high ambient temperatures or direct sunlight, can also interfere with accurate thermal measurements [8].

For the purpose of crack inspection, a straightforward method exists, namely the visual inspection, where trained personnel carefully examine the module for any visible cracks, chips, or other abnormalities. Nevertheless, relying on human perception may lead to subjectivity, inconsistency, and limitations in detecting microscopic flaws. Those are primarily due to the method's strong dependence on adequate illumination and viewing angle [9]. Human vision-based inspection also requires a considerable amount of time and manpower, making it less convenient for rapid or large-scale inspections. [10,11]. Advancements have been made to mitigate those shortcomings, such as a novel automated system with a scanning camera operating under high-intensity illumination [12,13] or the unmanned aerial vehicle (UAV)-assisted inspection enhanced by machine learning algorithms [14,15]. Still, alternative methods that are independent of optical factors will advantageously accommodate many practical cases with irregular illumination and limited field of view. Accordingly, the technique proposed in the present work attempts to address these issues using mechanical/acoustic waves that interrogate the physical structure of the material itself, thereby eliminating the visual constraints.

Ultrasonic methods offer automated solutions to the problems associated with visual inspection for mechanical defect detection. One technique implemented in the solar module manufacturing industry is resonance ultrasonic vibration (RUV), which swiftly recognizes defective solar cell wafers [16,17]. However, RUV works only on wafer inspection, whereas the present work aims to evaluate the entire solar photovoltaic module assembly. Another ultrasonic-based method closely relevant to our purpose is the ultrasonic c-scan method, which has been an industrial standard for mechanical defect inspection in various materials and dimensions. Nevertheless, it has a significant drawback of being time-consuming, which is unfavorable for a quality control process in a high throughput production line or an on-site inspection of a large-scale installations such as solar farms.

Ultrasonic Lamb waves are another promising alternative to the traditional ultrasonic methods for inspecting solar PV modules. It leverages the long-range detection characteristic of Lamb waves to overcome the speed constraint of the conventional ultrasonic c-scan. In the conventional c-scan approach, bulk ultrasonic waves probe the material in front of the transducer's face, generating echoes that serve as measurement feedback. Consequently, each recorded measurement corresponds to the material's condition at the point of the transducer's placement. In contrast, the proposed method leverages the advantages of Lamb waves, which propagate laterally across the structure, providing extensive area coverage. These laterally propagating waves contain valuable information about the material they interact with during their travel, which can be extracted by recording the signals at other locations on the plate. Fig. 1 illustrates the difference between bulk waves and Lamb waves. Detailed descriptions of Lamb waves fundamentals are available elsewhere, including in classical textbooks by Viktorov [18], Rose [19], and many other sources.

This paper intends to systematically outline the development of a Lamb waves (LW) scanning method for detecting cracks in the front glass of solar modules. This type of defect is one of the leading failure modes in solar modules in general [20,21]. Cracks initiate and grow during the operation due to mechanical loadings and impacts, such as those induced by wind, snow, and hail [22]. Additionally, non-operational factors also contribute to the occurrence of glass cracks, resulting from mishandling during transportation, installation and maintenance [23]. In general, the LW-based approach outlined in this work is applicable for module inspection throughout its lifecycle. Furthermore, automated measurement is possible by integrating the technique with a mobile robotic platform that is adaptable to the modules' installation conditions [24]. In this work, an automated LW inspection concept is demonstrated using a scanner machine. The closest implementation of this concept may find its place in a quality control process in a production line. Although the glass crack is not a significant failure mode to occur during this stage, but inspecting with this technique may provide extra layer of assurance. Nonetheless, the ultimate goal of this report is to demonstrate the primary working principle and performance, with the visionary aspiration of adopting the technique for other stages in the lifecycle with a higher risk of crack occurrence, such as during installation and periodic maintenance activities.

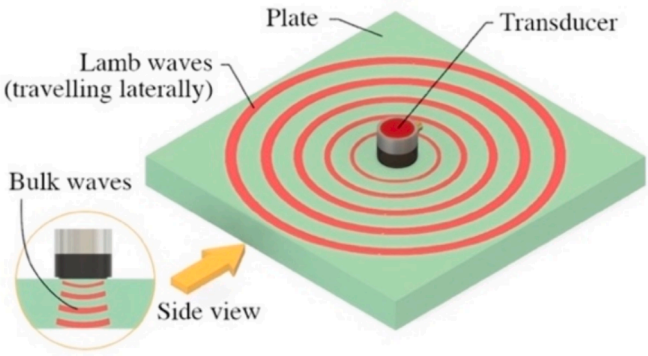

Fig. 1. Illustrations of the bulk waves traveling thickness-wise (used in conventional c-scan) and the Lamb waves traveling outwards from the excitation point, lateral to the plate's main plane.

Conventional c-scan can resolve cracks to a micro level beyond human vision, yet as stated before, the measurement is time-consuming. The developed LW scan method can detect cracks, even those barely visible to the human eye, but at a significantly faster measurement speed than the conventional method. One should note that, in this paper, the technique is implemented on a thin-film type solar panel. The application of this technique to the crystalline Si module requires a separate study due to the different structure in which the waves propagate. The structural aspects include the significantly thicker Si layer and the presence of conductive strips (busbars and fingers). Nonetheless, once the characteristics of the structure and the impact of defects on the wave behavior have been recognized, an approach similar to the one described in this paper can be followed. Indeed, the measurement parameters for damage detection on a specific structure, such as the measurement orientation, the selected wave modes, and the damage indicator threshold may vary specific to the structure.

2. Overview of the method

The specimen investigated here is a solar photovoltaic module (SHARP NA-E135-L5) of thin-film type with tandem cells, according to the product datasheet. The module contains cracks that occurred during product handling. That being said, the defects present in this specimen are natural and represent realistic conditions. Table 1 provides detailed information about the layer components of the specimen based on

Table 1
Layer materials of the specimen (ordered from the front glass panel to the back).

Layer	Material	Thickness
1	Front glass	3.2 mm
2	Transparent conductive oxide (TCO)	1.5 μm
3	a-Si + μcSi tandem cell	2.0 μm
4	Metal electrode	1.5 μm
5	EVA encapsulant	0.175 μm
6	Back glass	3.2 mm

product specifications and physical measurements.

A general arrangement of the experimental setup for the proposed Lamb waves (LW) scanning technique is exhibited in Fig. 2. The method involves two transducers (PANAMETRICS V103), one as the emitter and another as the receiver, placed at a fixed distance apart, d. The procedure to determine that emitter-receiver distance, *d*, will be discussed in Section 3. A function generator (Stanford Research Systems DS345) produces a tone burst signal that undergoes 10x amplification (Krohn-Hite 7500) before reaching the emitter, which excites Lamb waves in the specimen. In the LW scan setup, transducers are mounted on a holder and driven by the arm of an ultrasonic scanning machine (ITE/TransformNDT).

As explained earlier in the introduction, Lamb wave propagates away from the excitation point in the lateral direction of the plate's principal plane, not forward from the transducer's face as in the conventional pulse-echo c-scan. In a pitch-catch experiment, the propagating Lamb wave is captured at the receiver's side after interacting with the material along its way there. Therefore, the received waves contain information on material condition within the emitter-receiver path at each measurement position as the transducer pair moves to sweep the area. Signal recording, visualization, and scanner motion control are performed on the PC.

Before commencing the described LW scanning experiments, the distance between the emitter and receiver must be determined first. Then, with the transducers pair firmly assembled with the prescribed spacing, measurements are made on pristine and cracked regions of the specimen to extract damage indicator that discriminates those two conditions. Eventually, using the established criteria, the technique is applied for scanning a larger area to assess its crack detection performance. These stages are systematically elaborated in the ensuing sections.

3. Determining the spacing between transducers

A longer distance between transducers is desirable because it allows for a more extensive area to be covered within each scanning line stroke. However, stretching the emitter-receiver gap may raise some technical problems. One issue is wave attenuation due to elastic damping as the wave travels through the material, gradually losing its energy and diminishing the signal-to-noise ratio (SNR). Another concern is the inclusion of scattered waves from nearby discontinuities, such as edges or cracks, into the captured waveform due to the extended time of arrival of the direct signal. These unwanted waves can create interferences and obstruct the analysis of the primary signal.

To identify the most suitable transducer distance for our LW scan setup, we designed an experiment as depicted in Fig. 3. Referring to the illustration, the experiment uses two transducers, where the emitter remains stationary, and the receiver moves along a linear path driven by the scanner arm, capturing signals from points at various distances from the emitter. For all measurements conducted in this work, the emitter and receiver are positioned such that they maintain their line of sight parallel to the module's conductor gridlines. This setup allows recording the waves propagating in that specific direction. The intention is to eliminate any direction-dependent effect induced by the periodic pattern of metal conductor strips shown as gridlines from the front view of the module. Logically, one may intuitively infer that the waves traveling in the direction perpendicular to gridlines will repeatedly encounter the grid structure as they propagate. Meanwhile, those in the direction parallel to gridlines do not face such obstructions. At the intermediate orientations between those two directions relative to gridlines, the interaction between waves and structure varies with angles. More reliable and consistent results are expected by fixing the direction parallel to the gridlines throughout all measurements.

A contact emitter excites a 500 kHz sinusoidal vibration pulse following the settings on the function generator. The emitter and receiver are positioned at normal incidence in contact with the front glass surface, using water as a couplant. Note that in this experiment and other measurements in this work, water is introduced not by immersing the panel but only by wetting the front glass surface where the transducers are in contact. In certain industrial cases where the use of water or liquid is restricted, a dry-coupled wheel probe or air-coupled transducers can substitute the transduction method employed here.

The recorded waveform shape evolves with the distance due to the dispersive nature of Lamb waves and the presence of multiple Lamb modes propagating simultaneously, as shown in Fig. 4(a). However, the frequency content of those propagating waves, exhibited in Fig. 4(b), remains unchanged regarding the locations of the significant peaks, although the intensity of each band may differ. Consequently, frequency domain analysis is more appropriate as the basis for the defect identification method in this work.

Based on the findings from previous published work [25], our specimen exhibits four excited modes, namely mode 1, mode 2, mode 5, and mode 11. The cited publication scrutinizes the behavior of Lamb waves in the specimen and investigates the sensitivity of the propagating modes as they encounter cracks in structure. It thoroughly discusses the characteristics of waves in the specimen and the underlying physics of the observed phenomena. However, supplementary studies are required to convert the acquired knowledge into a pragmatic approach. Accordingly, the present work builds upon the findings of the previous report, incorporating comprehensive signal analysis and experimental design parameters to realize a tangible and practical inspection technique.

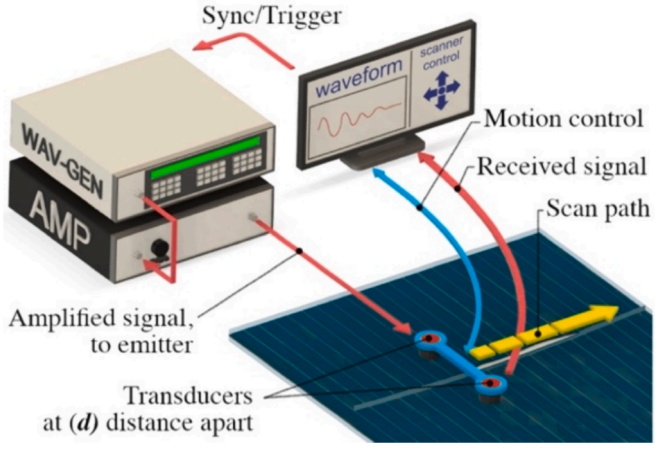

Fig. 2. Setup of Lamb Waves scans: a pair of transducers at a fixed distance is mounted on a scanner arm, performing a pitch-catch measurement procedure as the pair moves in a linear scan.

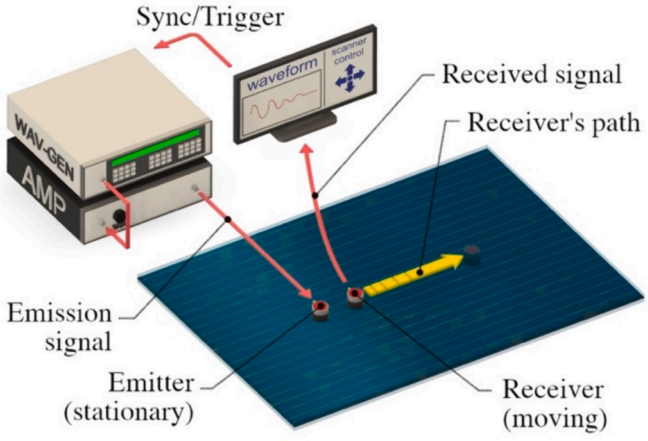

Fig. 3. Experiment to determine the distance between transducers for Lamb waves scan.

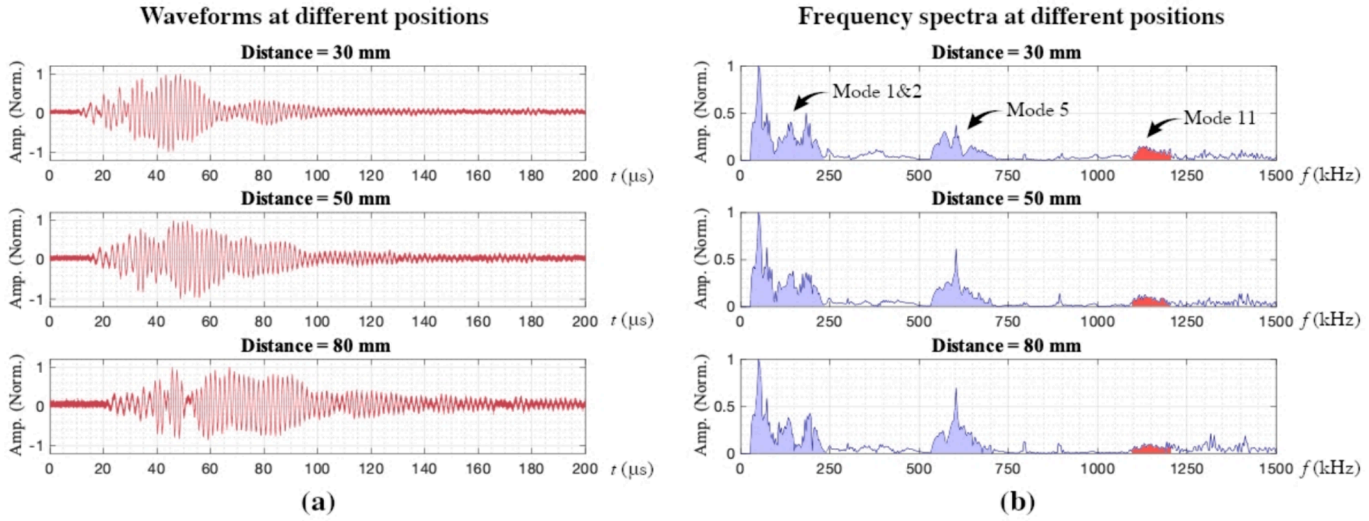

Fig. 4. (a) The shape of Lamb waves waveform varies with transducers distance; (b) The locations of significant frequency peaks are independent of distance, although only their intensities vary.

To stay consistent with the cited reference, the same numbering of mode designations are maintained to refer to the corresponding modes mentioned in this paper. These modes appear in the Fourier domain in Fig. 4(b) as dominant peaks at specific frequency ranges: Mode 1 and Mode 2 overlap each other within the 50 kHz – 230 kHz range; Mode 5 is observed between 550 kHz – 650 kHz; and Mode 11 is prominent in the 1100 kHz – 1200 kHz range. Among those modes, the main interest is directed towards Mode 11 due to its high sensitivity to cracks on the front glass, making it particularly significant for our analysis and discussion concerning crack detection in the front glass. The sensitivity of mode 11 to cracks in the front glass layer, i.e., the most convenient side for carrying out measurements, is due to the predominant energy distribution of this mode within that glass layer where the transducers are placed. This characteristic is exhibited by the power flow diagram in the cited work [25]. The wavelength of mode 11 falls within the range of 5.7—24.2 mm. It is important to note that this wide range of wavelength results from the dispersive behavior of this mode over the 1100—1200 kHz band. As the velocity varies substantially within this frequency regime, so does the wavelength. With the wavelength larger than the typical crack opening size, one may find it nonintuitive to use the waves for crack detection purpose. However, Lamb wave sensitivity is not merely determined by the correlation between its wavelength and the discontinuity dimension. It has been demonstrated that Lamb waves are sensitive to features that influence or disrupt their power flow in the structure, even if the dimension of the said features is less than the wavelength [26,27].

This work focuses on the front glass due to its higher probability of crack damage, but the fundamental concepts are adaptable for inspecting other layers. If the interest is in inspecting the back glass, the cited paper suggests utilizing mode 5 as the basis for investigating the damage indicator. Mode 5 is more sensitive to disturbances in the back glass due to its energy concentration in that region. Based on the same energy concentration argument, modes 1 and 2 are potential candidates for the detecting anomalies in the middle part of the panel sandwich, specifically, the solar cell layer and the encapsulant. A promising example comes from an evaluation of the adhesive layer in a laminated glass [28]. The paper reports that variations in the adhesive's properties affect the characteristics of Lamb modes with power flow concentrated near the midplane. In the case of a thin-film solar module with double-glass assembly, the analysis would not be as straightforward because the thin section between the glasses consists of multiple materials with non-uniform thicknesses, unlike the rather simple one-layer uniform adhesive in the laminated glass.

In order to determine the appropriate transducer spacing, it is essential to consider the signal strength on the receiver's side, particularly that of Mode 11 in the 1100 kHz – 1200 kHz range. Fig. 5(a) presents a color-scaled plot of spectrum intensities at the various distances between transducers, from 20 mm to 100 mm. It is evident from the color brightness profile that the intensity within Mode 11's frequency range gradually fades with distance.

Other modes at lower frequency regimes, however, behave in a manner that may cause issues for the actual measurement. Instead of steadily decreasing intensity, they form alternating highs and lows as the transducer's gap extends, showing patterns of bright and dark regions. This occurs due to the interference of waves reflected from the edge, being the only discontinuity feature nearby the measurement site since the experiment is conducted in a largely pristine area away from cracks. At each point, the reflected waves merge with the direct pitch-catch waves at a particular phase position, creating destructive or constructive interference that dictates the resultant amplitude of local displacements [29]. If these low-frequency modes were to be taken for the analysis, the phenomena would mislead the interpretation measurement results because the intensity variation is not related to the damage or intrinsic material response. Such alternating high and low peak regions do not appear in mode 11 because the high-frequency waves coming from the reflecting edges would have been substantially attenuated after traveling to the edge and rejoining the direct waves, causing less significant interference to the direct waves. That eventually becomes the advantage of using this higher-order mode over the lower ones.

The selection of transducer spacing is based on the Signal-to-Noise Ratio (SNR) level, taking the farthest distance that still has acceptable SNR for further signal analysis. SNR here is the energy spectral density (ESD) ratio of the signal of interest and the noise. The ESD of a bandwidth between frequencies *f1* and *f2* is an integration of Fourier intensity over the selected bandwidth, as expressed below [30]:

$$ESD = \int_{f1}^{f2} |X(f)|^2 df \tag{1}$$

where *X(f)* is the Fourier transform of the signal. According to Fig. 4(b) and Reference [25], for mode 11, the integration limits are from $f1 =$ 1100 kHz to $f2 =$ 1200 kHz, as suggested in the cited publication. On the other hand, the bandwidth representing noise is taken from 1450 kHz to 1500 kHz, where in that higher end of spectrum, the signal intensity is virtually negligible. That frequency range is justified as noise because it has approximately equally low levels of ESD across all measured

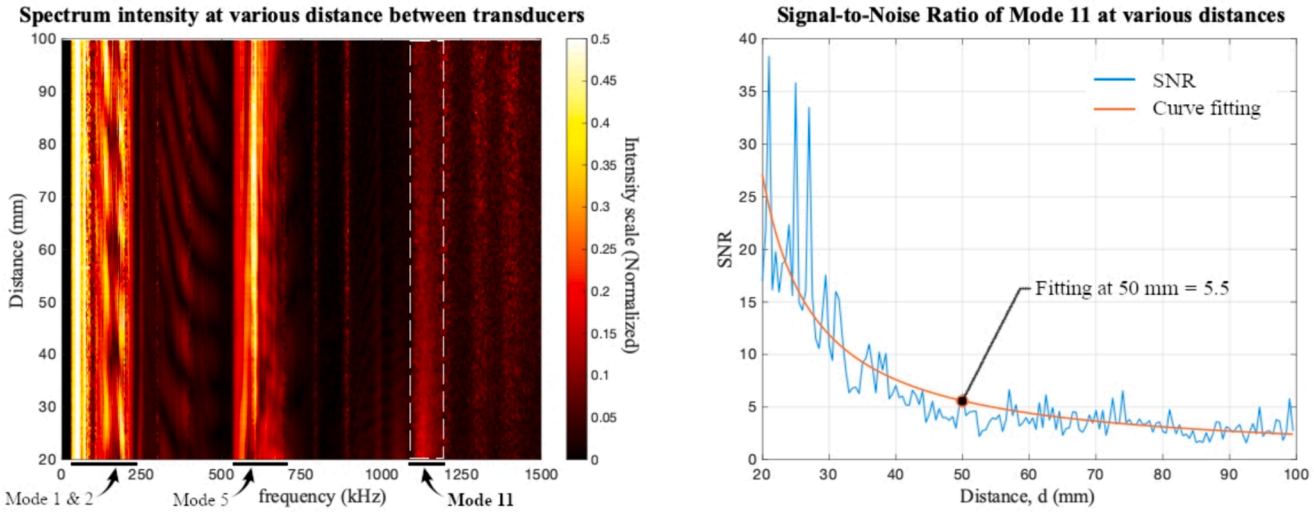

Fig. 5. (a) Intensity of spectrum at different distances showing that mode 11 diminishes as the distance increases; (b) Plot of Signal to Noise Ratio of mode 11 with curve fitting: at 50 mm, the SNR is 5.5 on the fitted curve. This distance is selected as the transducer spacing.

distances. Consequently, the SNR is calculated by dividing the ESD of mode 11 by the ESD of the noise ($SNR_{mode11} = ESD_{mode11} / ESD_{noise}$). The plot of values at all measured points and its fitted curve, are plotted in Fig. 5(b), showing that the SNR drops with distance due to material damping. Finally, the transducers spacing (d, in Fig. 1) of 50 mm is chosen in this work where at that distance the SNR is around 5.

The choice of SNR value in this experiment, and hence the spacing between transducers, is determined by considering instrument configuration and scanning conditions. These conditions include factors such as nonuniform couplant/water film thickness in the gap between transducer face and glass surface as well as the vibration of the scanner arm. If the scanning conditions are steady, it is possible to stretch the transducers spacing to an even larger distance. For instance, setting the spacing to 90 – 100 mm where the SNR eventually values flattens out at around 2.5, would work fine. However, in our experimental setup a larger SNR value guarantees a reliable signal strength, providing a margin of tolerance for unsteady operational conditions during the scanning process. When observing frequency peaks within the regime of mode 11 (the strip confined by the dashed lines) in Fig. 5(a), at the larger spacing between transducers, the contrast diminishes and becomes less distinguishable, especially relative to the higher frequency side.

4. Obtaining the damage indicator of a crack

This part of the work compares the measurement results of Lamb waves (LW) scan experiments on pristine and defective areas. During measurements, both transducers scans a straight path of 100 mm, and the received waveform is recorded every 1 mm, resulting in a dataset of 101 measurement positions (positions 0 to 100). In practice, the emitter and receiver are placed on a holder mounted on the scanner's arm, as illustrated in Fig. 2. This arrangement ensures that both transducers move together at a constant distance, d, when the machine scans a line. The transducer spacing, d, as selected in the previous section, is 50 mm. Identical to the excitation conditions in the previous section, the emitter excites a 500 kHz pulse, and the receiver captures signals that travel parallel to the gridlines. Subsequently, these time signals are processed in MATLAB to analyze the frequency spectrum.

The probes arrangement and signal emission settings described in Fig. 2 are applied to perform scans on three sections of different structural conditions. Photographs of the three measured sections are presented in Fig. 6(a, b, and c), with the following visually observed conditions: pristine (Section A), cracked along the section (Section B), and partially cracked (Section C). Notice that Section B has a part with a fine crack. The measurement results will reveal the intensity variations

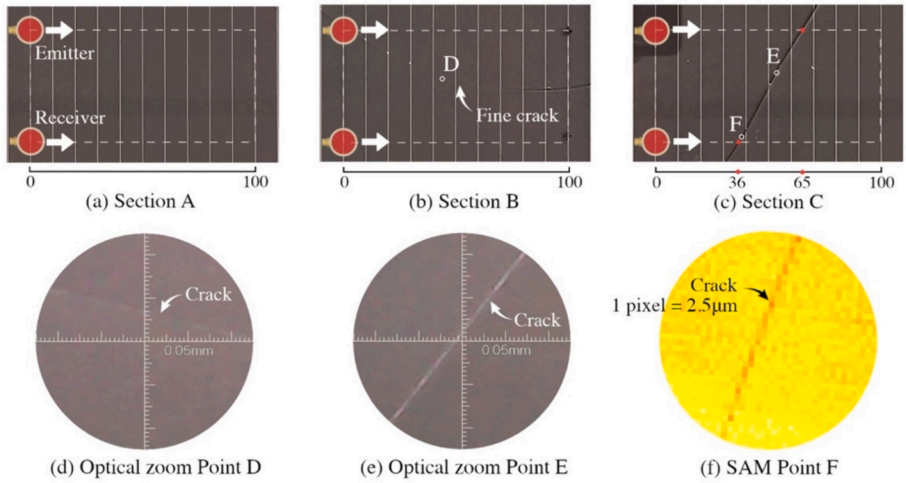

Fig. 6. (a, b, and c) The sections measured in the LW scan experiments to find damage indicators. (d and e) Optical microscope magnification of crack at the designated locations. (f) Scanning Acoustic Microscope (SAM) image of a typical crack.

of the damage-sensitive mode (Mode 11) that can indicate the presence of a crack.

Under an optical microscope (digital microscope), it is evident that the width of a fine crack in Section B, represented by Point D as enlarged in Fig. 6(d), is smaller than that in the location where the crack is visible, for example, Point E with its zoomed-in image in Fig. 6(e). Gauging the crack with the shown crosshair scale in images (d) and (e), the width of both cracks at points D and E are less than 0.005 mm (5 mm). Our optical microscope's maximum magnification power limits further enlargement. As a complementary measurement, another method is employed, namely Scanning Acoustic Microscopy (SAM). A point in Section C (Point F) is scanned with SAM, resulting in an image shown in Fig. 6(f). For this scanning attempt, acoustic microscopy is carried out with a 400 MHz transducer, and the resolution is 2.5 mm per pixel. Accordingly, since in Fig. 6(f), the crack line is only 1 pixel wide, then the crack width is 2.5 mm at most.

While, in general, it is possible to detect cracks visually using bare eyes, an optical microscope, and by evaluating the area topographically with SAM as shown in Fig. 6, these detection techniques also have their limitations. Regarding visual detection, the contrast of the crack line, hence the detectability, depends on the viewing angle and ambient light. Observing a crack at an orientation such that the inspector's viewing angle is directly parallel to the crack faces results in a poor contrast. This situation is exacerbated in the scenario of micro-cracks or fully closed cracks. Comparing Fig. 6(b) and 6(c), the crack in section C is more easily detected, not only due to its severity but also because of the direction of ambient lighting that creates reflections and shadows in its vicinity. On the other hand, in section B, a portion of the crack line is virtually undetectable due to the combination of its fine size, viewing angle and the absence of ambient light effects. The issue of contrast variability also persists under the microscope. In section C, the crack that is undetectable by bare eyes exhibits only a faint line in its corresponding microscope image (Fig. 6(d)), as compared to the one from section C (Fig. 6(e)). Lighting is a crucial part of visual inspection, but the operator's perceptiveness also plays substantial role in locating the crack [31]. If the human factor is taken into account, the probability of non-detection increases, particularly in the inspection of cracks under unfavorable angles and lighting conditions.

Concerning the topographic evaluation performed by means of SAM as depicted in Fig. 6(f), its sensitivity to minuscule physical irregularities on the surface becomes the main advantage. The technique effectively detects any ridge or opening due to a crack. However, the working principle of the technique itself leads to an inherent limitation that the detection only occurs if the damage creates a physical feature on the surface. If the damage is beneath the surface, such as a crack that initiates from the inside and does not fully propagate all the way to the outer surface, then the damage will not be identifiable in the SAM image.

Besides their advantages, both optical and acoustic microscopy share a common shortcoming: their advanced capabilities can only be utilized on one small piece of area at a time. Consequently, both techniques are not viable for large area inspection, although they serve excellently for a detailed examination targeting small area of interest. This fact leaves us with the manual, naked-eyes visual inspection as the primary method relevant to the crack detection of a full-size solar module, which alternative is pursued through Lamb waves-based strategy explored in this paper.

The LW measurement results from those sections displayed in Fig. 6 (a, b, c) are plotted in Fig. 7. To emphasize that analysis in the frequency domain is the more suitable approach over the seemingly straightforward time domain analysis, the peak-to-peak amplitude of the acquired time signals from all sections is plotted in Fig. 7(a). From that plot, it can be confirmed that merely taking the amplitude of the received signal in the time domain is ineffective for crack detection since there is no strong correlation between the level of amplitude and the presence of a crack. It is because the propagating wave consists of multiple modes, and not all of them are sensitive to cracks. Low order modes (such as Mode 1 and 2) at low frequency (below 250 kHz), being the predominant energy carriers in the spectrum, pass through the crack without a significant decay in their intensity [32,33] because they are not sensitive to the crack. Therefore, the overall time domain amplitude is relatively uncompromised as the energy drop of the crack-sensitive mode (that lies in the high-frequency regime), which is less dominant in the spectrum, is not manifested in the waveform.

In contrast, frequency domain analysis regarding the ESD ratio can indicate a crack. The graphs in Fig. 7(b) plot the ESD ratio of mode 11 from measurement data obtained by scanning the sample sections. There, the ESD ratio is expressed as a percentage that implies the proportion of mode 11 in the spectrum of the received signal. Comparing the plots of three measured sections, it is evident that the percentage level of the undamaged section (Section A) is always higher than the damaged section (Section B) at all points throughout the scanning experiment. Furthermore, since the graph itself is a collection of measurement results at every 1 mm for the entire length of the 100 mm scan, each plot can be interpreted as a series of 101 data points (from point 0 to point 100) that represents repeated measurements in a particular condition of the structure, either pristine or cracked. Hence, they may provide descriptive statistics to determine the threshold that discriminates between the pristine and defective sections of the inspected structure.

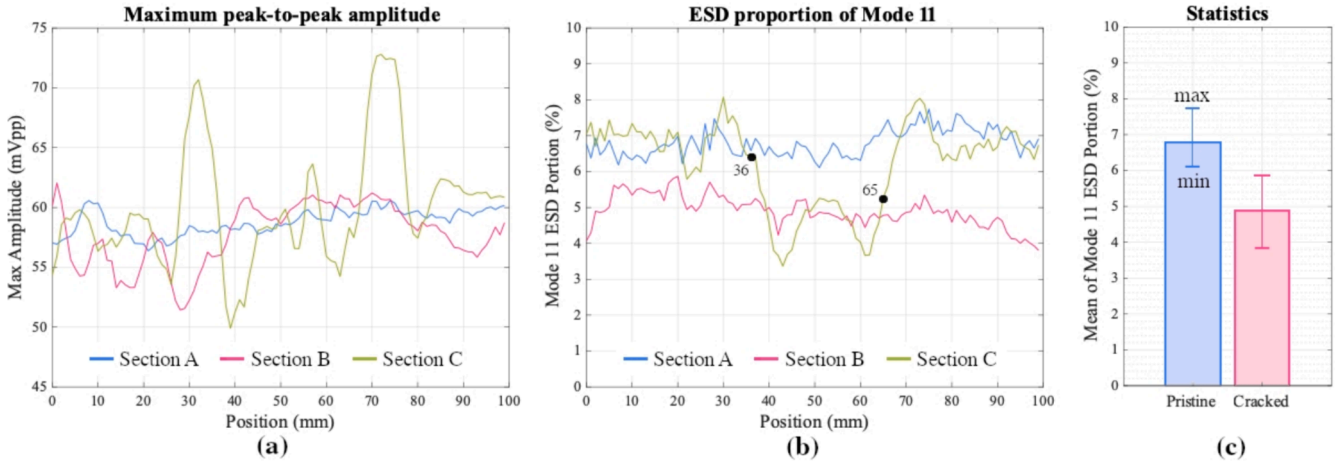

Fig. 7. (a) The maximum peak-to-peak amplitudes of time signal waveforms do not indicate material conditions. (b) The proportions of mode 11 ESD present clear indications of a crack. (c) Mean values of ESD levels show the gap between the two contrasting conditions.

The statistics of data from pristine and defective areas convincingly show distinctions between the two conditions, as shown in Fig. 7(c). The mean of the data series from measurements on the undamaged part is nearly 7 %, and that of the cracked section is 5 %. In addition, the maxima and minima of data sets from the two sections do not overlap. Based on the statistics, it is justifiable to set 6 % of Mode 11 ESD proportion as the threshold below which a measurement instance is considered "cracked.".

A crucial finding from the measurement results in Fig. 7(b), particularly in Section B, highlights the capability of the utilized technique to identify cracks even when they are not readily perceptible, as depicted in Fig. 6(b and d). The percentage levels from the measurements in Section B are consistently lower than that in Section A across all data points, even in the part where the crack is barely visible in Section B. This fact underlines that the LW inspection offers benefits over manual visual inspection since it can detect cracks imperceptible by human eyes. As described before, visual inspection can be less reliable in the case of fine cracks under unfavorable observation conditions due to lighting, viewing angle, or operator's perceptiveness factors. On the other hand, LW detection is based on the physical condition of the structure, regardless the aforementioned factors.

The measurement results from Sections A and B have demonstrated the ability of this technique to differentiate the undamaged and cracked sections based on the distinguishable levels of mode 11 ESD. Another realistic circumstance in the inspection is a crack situated only in a short segment of the scanning length, as in Section C, shown in Fig. 6(c). The crack exists only from 36 mm to 65 mm in that 100 mm long scan. Numerous studies have conducted Lamb wave scans on partially defective samples, such as detecting delamination spots [34], mechanically impacted areas [35], or holes [36] in plate structures. However, most investigations focus on evaluating samples with artificial defects wholly located between the transducers. In the present study, the crack extends from one transducer's scan trajectory line to another, and the crack itself is oriented at an angle relative to the line of sight of the transducers. To the authors' knowledge, such conditions have not been much explored in similar research on Lamb waves scanning.

A distinctive pattern appears in the Mode 11 ESD plot of section C in Fig. 7(b), in vicinity of the cracked zone, showing spikes of the value near the actual crack position. To explain the mechanism, an illustration of the pitch-catch condition around a crack line is presented in Fig. 8. The scenario is comparable to the section C crack image in Fig. 6(c) whose ESD is plotted in Fig. 7(b) as the green colored line.

Obviously, at a position where there is no crack between transducers and none of the transducers are nearby the crack line, Fig. 8(a), the ESD level reading will be on the upper side of the threshold. As a transducer comes close to the crack but that crack line does not lie between two transducers, Fig. 8(b), the ESD percentage level increases. The event corresponds to the spikes in section C plot at around 30 mm and 73 mm in Fig. 7(b). The spike occurs due to the relatively strong high-frequency portion in the waves reflected by the nearby discontinuity. These reflected waves retain sufficient energy upon reception because the waves only travel a short distance from reflector to the receiving transducer. Conversely, when the reflector is situated far from the transducer, the high-frequency part of the reflected waves experiences attenuation as it travels through the material. As a result, it contributes negligibly to the received signal. In summary, the influence of reflected waves on the proportion of high-frequency components is significant only when the transducer is near the crack.

There is a transient in the ESD level within the transitional region like the one exemplified in Fig. 8(c), where the transducer (receiver) engages both sides of the crack line. The gradual decline of the ESD level is attributed to the variation of vibration energy transfer between the receiver and the glass surface divided by a crack. As the scanning progresses, the receiver completely clears the crack line, see Fig. 8(d). At this position, the ESD level reading is below the threshold. If the scan continues to the right direction from this point, then the emitter will reach the crack line and undergo transition. In that case, the ESD level gradually rises again with a similar mechanism as explained earlier during the receiver's transition.

Revisiting Fig. 6(c), in the scanned section, the crack exists in the region from 36 mm to 65 mm. However, in the corresponding plot of Section C, annotated by dots in Fig. 7(b), the points where the ESD level drops and recovers are not precisely at the onset and the end of the cracked zone. The factor that affects this discrepancy is the size of the transducers, having a diameter of 13 mm. When a transducer passes over a crack, a displacement equal to its diameter is needed to completely shift the transducer from one side of the crack line to the other. It results in a gradual change in ESD value instead of an immediate transition from high to low values (or low to high in the case of transducers leaving a crack line). One way to alleviate this issue is by using transducers with a small or pointed face, as proposed in reference [37]. Alternatively, another approach, which compensates for the diameter of the transducer, has been successfully applied in this work and is described in the following passage.

In the proposed technique, only binary detection is expected: either "cracked" or "not cracked". Thus, the gradually changing ESD magnitude when the transducer crosses over the crack line must be binarized into the two extremes, either above or below the crack indicator threshold. This adjustment is accomplished by compensating with one-half diameter (radius) of the transducer. Note that one-half diameter and radius can be used interchangeably for this purpose; the preference in this paper is solely because transducer manufacturers mostly specify the size in terms of diameter.

The rationality behind this compensation strategy is based on the assumption that the indicator threshold is most likely to be reached after the crack passes at least halfway across the transducer face, or simply around the center of the circular transducer. Before that point, the ESD decreases but remains on the upper side of the threshold limit, even

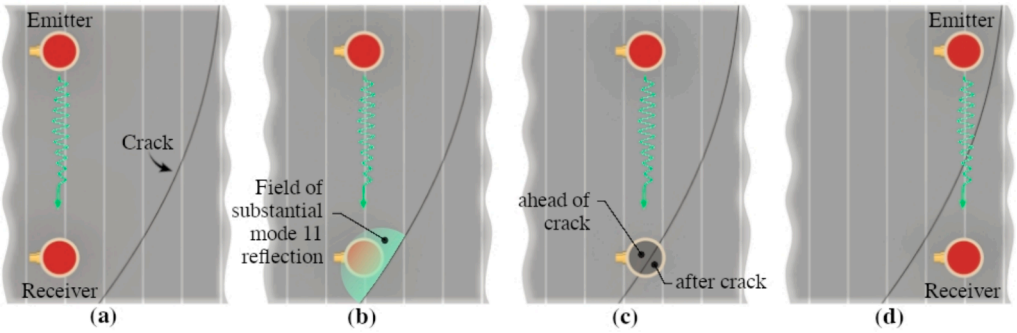

Fig. 8. Illustrations of pitch-catch scenarios: (a) No crack between transducers; (b) A transducer is close to the crack that the reflection of Mode 11 substantially contributes to the captured signal; (c) At the transition zone, transducer face covers both sides of crack line, causing transient in Mode 11 ESD level; (d) The crack is between the transducers and none of transducers is over the crack line.

though the transducer has traversed the crack. This occurs because only the smaller portion of the face area has crossed the crack line. Therefore, it is reasonable to assume that the positions up to a distance of one-half diameter before and after the point where ESD just falls below the threshold are considered as "cracked", since the transducer indeed starts to engage or leave the crack at its periphery, which is essentially one-half diameter away from the center. Demonstrating this approach in an experimental procedure, as discussed in the subsequent section, will further clarify its utility.

5. Implementation of the LW technique for scanning a larger area

The effectiveness of this method in recognizing cracks has been demonstrated in the previous section through a single-pass scanning measurement. However, in actual inspections, the evaluated areas typically have sides with lengths of several times the transducer spacing. Consequently, multiple passes of the probes in the setup shown in Fig. 2 are needed to encompass such large areas. The scanning movement of the probes resembles that of the conventional c-scan, but the number of passes required to cover a given area is significantly reduced. This reduction occurs because each scan pass with the LW method already covers a particular section of the evaluated area, rather than just a line as in the conventional c-scan. This feature of the LW scan technique is its main advantage over the conventional c-scan: with fewer passes, the measurement time will be significantly faster.

As an implementation test of the developed LW scanning concept, we evaluated a 200 mm x 200 mm area depicted in Fig. 9(a). Looking closely at the image, a crack line extends from the left edge at the vertical scale of 175 mm to the top edge at 130 mm on the horizontal scale. A conventional c-scan technique at 1 mm resolution would require 201 scan passes to cover that area. However, with the Lamb waves technique presented in this work, the number of passes is reduced to only 4 because each pass already covers a width of 50 mm. Each scanning pass is designated as a row in Fig. 9, hence there are 4 rows. In the plot, the transducers' spacing of 50 mm is translated as the vertical-axis resolution in the image, while the horizontal-axis resolution is 1 mm. Furthermore, it can be deduced that the scan image of a 200 mm x 200 mm area comprises four rows of rectangular strips of 50 mm width (vertical) and 200 mm length (horizontal).

Since cracks are unacceptable in solar panel production and installation stages, and irreparable in the operation, detecting their presence without knowing detailed information about their size or orientation is sufficient. The inspection outcome is therefore binary: either the panel is non-defective and passes the quality control stage, or it is cracked, leading to product rejection or replacement. To provide such information, the generation of the scanned image for crack assessment relies on the following two conditions. If the mode 11 ESD percentage is below the 6 % threshold, the corresponding section is marked as "cracked." Conversely, if the percentage exceeds the threshold, it is a "no crack" instance. The resulting image can be rendered with colors, as shown in Fig. 9(b and c), where green and red signify non-cracked and cracked, respectively.

Once the image is rendered, by looking at Fig. 9(b), one can readily spot discrepancies: although the crack is continuous in the specimen, the resulting LW scan is intermittent. These fragmented strips appear because the consistently low values of ESD level occur only when both transducers completely clear the crack so that the crack line is situated between the transducers. When a transducer is just entering the crack zone, and its vibrating face is over the crack line, the recorded ESD level has not decreased sufficiently below the threshold. It is because some portion of the transducer face still excites or receives Lamb waves in the section where there is no crack between the two transducers. This issue has been addressed in the preceding section through the illustration in Fig. 8.

To account for the transducer diameter issue, in the plotting routine, we impose a compensation length of 6 mm (equivalent to one-half the transducer diameter) before and after the point where the ESD threshold (6 %) is reached either from the higher values (when ESD is gradually decreasing) or lower values (when it is increasing). Briefly reiterating the explanation from the previous section on the discussion of Fig. 8, the one-half diameter adjustment is taken under the assumption that when more than half of the transducer face is still located before the crack, most of the vibration energy is transferred in the region without the crack in the line of sight between the transducers. Thus, for instance, when the receiver is over the crack, as shown in Fig. 8(c), the transducer is already in the crack zone, but the ESD level has not yet dropped below the threshold. In that case, the system will not register such a position as "cracked," yielding misinterpretation.

Implementation of the one-half diameter adjustment routine extends the "cracked"-interpreted segment (red colored rectangles in Fig. 9) by 6 mm on both sides (before and after detection). This results in a significantly enhanced accuracy in crack mapping, as shown in Fig. 9(c). Therefore, it has been demonstrated that the discrepancy in crack indications due to the transducer size factor can be corrected through an adjustment routine that considers the associated dimension, in this case, the diameter.

6. Accuracy of the technique

Despite the substantial refinement after applying the transducer diameter compensation procedure, the resulting image still contains

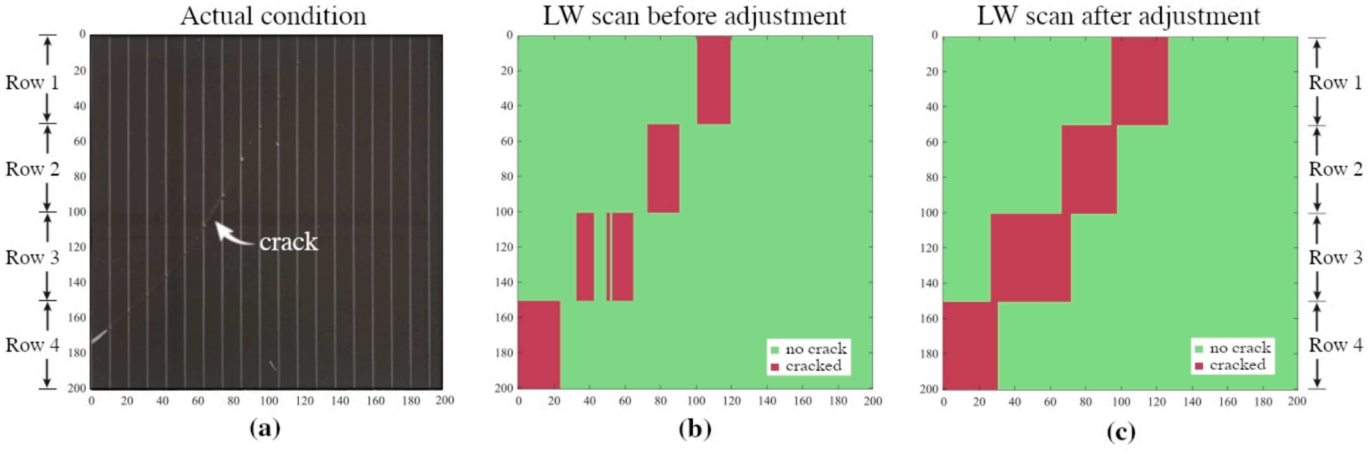

Fig. 9. (a) Actual condition of the evaluated area with a crack extending from the left edge at 175 mm to the top edge at 130 mm; (b) LW scan image before adjustment to compensate for transducer diameter size; and (c) LW scan after adjustment.

some misdetections. The image from the LW scan is overlaid on the picture of the measured section in Fig. 10 to facilitate accuracy assessment. In that figure, there are instances that the color indications incorrectly describe the actual state. As pointed out in that image, some crack indications (red colored) are elongated beyond the crack endpoints in that scanning row's boundary. The zoomed-in image in Fig. 10 demonstrates the misdetection events with the white-shaded regions marking the part where undamaged sections are incorrectly detected as cracked.

At a scanning resolution of 1 mm, the 200 mm x 200 mm area consists of 800 measured positions (4 scan rows of 50 mm width each, 200 measurement positions per row at 1 mm interval). The accuracy evaluation is based on the number of correctly and incorrectly identified measurement positions. For example, in Row #1 in Fig. 10, the horizontal axis positions of 95 – 97 mm and 126 mm are falsely identified as cracked because they are actually in the pristine region. Misdetections also occur in the other rows, marked with the white shadings at the end (s) of red rectangles.

The accuracy is calculated using a formula commonly utilized in diverse fields related to binary diagnostics or predictions to quantify the accuracy of a particular technique [38–40]:

$$\text{Accuracy} = (\text{TP}+\text{TN})/(\text{TP}+\text{TN}+\text{FP}+\text{FN}) \quad (2)$$

Descriptions of parameters and the corresponding values in Equation (2) are provided in Table 2. Referring to Fig. 10, TP value is the number of positions with red color, TN is green, FP is white shaded positions, while FN is non-existent because there is no undetected crack event.

The calculated accuracy of 98 % from our experimental scan proves that the LW scan technique is effective for crack detection because it can correctly determine the condition of the area at nearly all the inspection points. While error exist, it does not distract the testing decisions based on the produced scan image. All misdetections occur adjacent to the area with real cracks and never elsewhere. In brief, false crack detection only occurs if a real crack exists. Therefore, its appearance is predictable. In addition, since the presence of a crack will fail the solar module in quality control regardless of its location or severity, a minor dimensional deviation in crack mapping has an insignificant impact on the pass-fail assessment process.

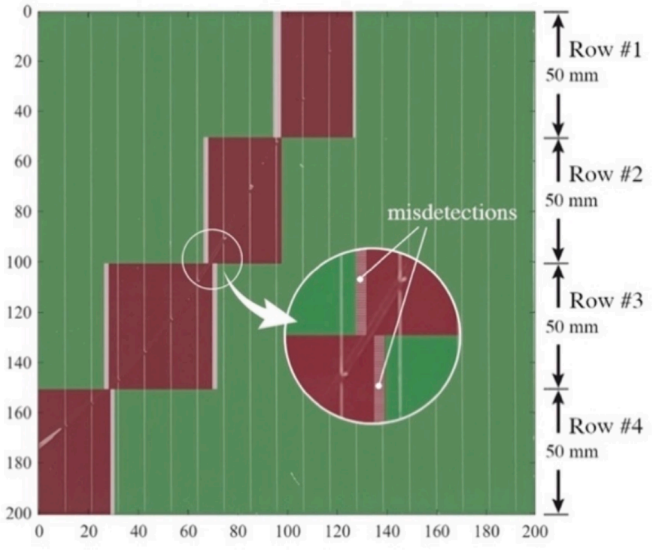

Fig. 10. Superimposing LW scan image over the real picture of inspected area for accuracy evaluation.

Table 2
Definitions of terms involved in accuracy calculation.

Parameter	Description	Value
TP (True Positive)	Cracked area is interpreted as cracked	122
TN (True Negative)	Non-cracked area is interpreted as non-cracked	662
FP (False Positive)	Non-cracked area is interpreted as cracked	16
FN (False Negative)	Cracked area is interpreted as non-cracked	0
Accuracy	**Ratio of correct prediction or detection**	**98 %**

7. Recommendations to improve the practicality of the technique

Besides accuracy, another aspect worth discussing is the measurement speed or rate. The proof of concept outlined in this paper works with 50 mm spacing between transducers. Therefore, to cover a full-size 1000 mm x 1400 mm panel, it requires 28 series of 1000 mm line-scans. At a scan velocity of 30 mm/s, as practiced in our experiment, it takes around 15 min to finish a panel. Admittedly, a faster inspection speed is desired to make the technique more attractive. Improvements in this sector are possible by extending the spacing between transducers, increasing the scanner arm motion velocity, and performing the scan with multiple pairs of transducers, each accompanied by some relevant considerations. Wider spacing between transducers can be facilitated by employing apparatus capable of generating clean signal with high amplitude to yield a sufficiently strong signal-to-noise ratio at the receiver side. However, one may anticipate that this speed enhancement through wider spacing between transducers is gained at the expense of the resolution of the area mapping.

Another intuitive way to increase the scanning speed is by setting a higher velocity for the scanner arm motion. However, there is a prerequisite for this speed tuning attempt, i.e., a high sampling rate data acquisition device which serves as the signal recorder. Faster scanning motion demands a data acquisition board with a higher sampling rate specification, otherwise the system is unable to capture the complete signal for each acquisition point, particularly in high-resolution scanning. Our system is equipped with a 2 Msamples/s sampling rate data acquisition board (National Instrument AL12200). Acquisition boards of significantly higher sampling rate in excess of 2 Gsamples/s are exist, allowing for a higher scanning speed.

The next option to attain rapid scanning is by utilizing multiple pairs of transducers, instead of only one pair as practiced in this conceptual work. Consider a series of transducers pairs, arranged such that they span the module lengthwise (or widthwise). If all pairs scan simultaneously, then an inspection of the whole area will be completed by only a one-way linear scan in the widthwise direction (or lengthwise if the transducers array span widthwise). This setup requires a generous quantity of transducers. For instance, to span a length of 1400 mm with 50 mm spacing between transducers, 28 pairs are needed, thus 54 units of transducer. Additionally, a multichannel waveform generator and acquisition board are needed. Despite the intensive requirement of instruments, the expected improvement is enormous. Envisaging this setup for inspecting the full-size panel used in this work, the previously mentioned 15-minutes duration will shrink to less than one minute, as only a single scanning pass is required.

Several avenues for improvement, as previously discussed, offer opportunities to optimize the practicality of this technique, with trade-off between performance gain and cost impact due to the additional instrumentations and complexities required to fine tune the system.

8. Conclusion

This work has demonstrated the use of Lamb waves (LW) scanning for crack detection in the front glass of solar modules. The technique is an alternative to the vision-based inspection approach that may be affected by the lighting conditions and human's visual perceptiveness.

Unlike the common Lamb waves approach that exploits low-order, fundamental modes, the current technique employs a higher-order mode that is more sensitive to cracks in the front glass portion of the solar module layup. A damage indicator based on the energy spectral density (ESD) proportion of that target mode has been established, setting a specific threshold that discriminates between cracked and undamaged cases.

The damage indicator is implemented in a LW scan imaging routine, and a measurement attempt on the larger area containing a crack is performed, yielding a satisfactorily accurate result. While some errors exist, they are not necessarily detrimental to the decision-making process in a quality control procedure that demands binary outcomes: either the module is perfectly undamaged (pass) or contains a crack (fail).

As a closing remark, Lamb wave characteristics are influenced by the materials used in the layup and the thickness of each layer. Therefore, adjustments to quantitative parameters are required when applying the technique to other types of solar modules, such as the c-Si photovoltaic modules. Nevertheless, the fundamental concept and working principles remain functional.

CRediT authorship contribution statement

Dicky Silitonga: Conceptualization, Formal analysis, Investigation, Methodology, Validation, Visualization, Writing – original draft. **Nico F. Declercq:** Supervision, Validation, Writing – review & editing. **Fodil Meraghni:** Writing – review & editing. **Bertrand Boussert:** Writing – review & editing.

Declaration of Competing Interest

The authors declare that they have no known competing financial interests or personal relationships that could have appeared to influence the work reported in this paper.

Acknowledgement

The authors express their gratitude towards Georgia Tech Europe; and to SHARP Energy Solutions Europe for providing product details.

References

[1] J. Ramanujam, D.M. Bishop, T.K. Todorov, O. Gunawan, J. Rath, R. Nekovei, E. Artegiani, A. Romeo, Flexible CIGS, CdTe and a-Si: H based thin film solar cells: A review, Prog. Mater. Sci. 110 (2020) 100619, https://doi.org/10.1016/j.pmatsci.2019.100619.

[2] T.D. Lee, A.U. Ebong, A review of thin film solar cell technologies and challenges, Renew. Sustain. Energy Rev. 70 (2017) 1286–1297, https://doi.org/10.1016/j.rser.2016.12.028.

[3] T. Feurer, P. Reinhard, E. Avancini, B. Bissig, J. Löckinger, P. Fuchs, R. Carron, T. P. Weiss, J. Perrenoud, S. Stutterheim, S. Buecheler, A.N. Tiwari, Progress in thin film CIGS photovoltaics – Research and development, manufacturing, and applications, Prog. Photovolt. Res. Appl. 25 (2017) 645–667, https://doi.org/10.1002/pip.2811.

[4] P. Čulík, K. Brooks, C. Momblona, M. Adams, S. Kinge, F. Maréchal, P.J. Dyson, M. K. Nazeeruddin, Design and cost analysis of 100 MW perovskite solar panel manufacturing process in different locations, ACS Energy Lett. 7 (2022) 3039–3044, https://doi.org/10.1021/acsenergylett.2c01728.

[5] M.J. (Mariska) de Wild-Scholten, Energy payback time and carbon footprint of commercial photovoltaic systems, Sol. Energy Mater. Sol. Cells 119 (2013) 296–305, https://doi.org/10.1016/j.solmat.2013.08.037.

[6] Á.H. Herraiz, A.P. Marugán, F.P.G. Márquez, Chapter 7 - A review on condition monitoring system for solar plants based on thermography, in: M. Papaelias, F.P.G. Márquez, A. Karyotakis (Eds.), Non-Destr. Test. Cond. Monit. Tech. Renew. Energy Ind. Assets, Butterworth-Heinemann, Boston, 2020: pp. 103–118. 10.1016/B978-0-08-101094-5.00007-1.

[7] L. Hernández-Callejo, S. Gallardo-Saavedra, V. Alonso-Gómez, A review of photovoltaic systems: Design, operation and maintenance, Sol. Energy 188 (2019) 426–440, https://doi.org/10.1016/j.solener.2019.06.017.

[8] M.S. Jadin, S. Taib, Recent progress in diagnosing the reliability of electrical equipment by using infrared thermography, Infrared Phys. Technol. 55 (2012) 236–245, https://doi.org/10.1016/j.infrared.2012.03.002.

[9] V. Sugumaran, Fault diagnosis of visual faults in photovoltaic modules: A Review, Int. J. Green Energy 18 (2021) 37–50, https://doi.org/10.1080/15435075.2020.1825443.

[10] M. Aghaei, F. Grimaccia, C.A. Gonano, S. Leva, Innovative automated control system for PV fields inspection and remote control, IEEE Trans. Ind. Electron. 62 (2015) 7287–7296, https://doi.org/10.1109/TIE.2015.2475235.

[11] S. Hassan, M. Dhimish, Enhancing solar photovoltaic modules quality assurance through convolutional neural network-aided automated defect detection, Renew. Energy 219 (2023) 119389, https://doi.org/10.1016/j.renene.2023.119389.

[12] Solar Panel Inspection, K-Space Assoc. Inc. https://k-space.com/industrial-metrology/solar-panel-inspection/ (accessed March 26, 2024).

[13] L. Rupert, C. McDonald, M. Soghrati, R. Angiuli, D. Barlett, G. Guerrero, Laser based metrology for First Solar Series 6 module manufacturing packaging process control. https://www.nrel.gov/docs/fy18osti/72423.pdf (accessed March 26, 2024).

[14] N.V. Sridharan, V. Sugumaran, Convolutional neural network based automatic detection of visible faults in a photovoltaic module, energy sources part recovery util, Environ. Eff. (2021) 1–16, https://doi.org/10.1080/15567036.2021.1905753.

[15] Z. Yahya, S. Imane, H. Hicham, A. Ghassane, E. Bouchini-Idrissi Safia, Applied imagery pattern recognition for photovoltaic modules' inspection: A review on methods, challenges and future development, Sustain. Energy Technol. Assess. 52 (2022) 102071, https://doi.org/10.1016/j.seta.2022.102071.

[16] W. Dallas, O. Polupan, S. Ostapenko, Resonance ultrasonic vibrations for crack detection in photovoltaic silicon wafers, Meas. Sci. Technol. 18 (2007) 852, https://doi.org/10.1088/0957-0233/18/3/038.

[17] A. Belyaev, Yu. Emirov, S. Ostapenko, I. Tarasov, V. Verstraten, M. Van Dooren, P. G. Fumei, G. Van Veghel, P. Bentz, A. Van Der Heide, Yield enhancement for solar cell manufacturing using resonance Ultrasonic vibrations inspection, in: 2009 34th IEEE Photovolt, Spec. Conf. PVSC 2009 (2009) 001918–001921, https://doi.org/10.1109/PVSC.2009.5411565.

[18] I.A. Viktorov, Rayleigh and Lamb Waves, 1st ed., n.d. https://link.springer.com/book/9781489956835 (accessed September 21, 2022).

[19] J.L. Rose, Ultrasonic Waves in Solid Media, Cambridge University Press, 1999.

[20] J. Kim, M. Rabelo, S.P. Padi, H. Yousuf, E.-C. Cho, J. Yi, A review of the degradation of photovoltaic modules for life expectancy, Energies 14 (2021) 4278, https://doi.org/10.3390/en14144278.

[21] D.C. Jordan, T.J. Silverman, J.H. Wohlgemuth, S.R. Kurtz, K.T. VanSant, Photovoltaic failure and degradation modes, Prog. Photovolt. Res. Appl. 25 (2017) 318–326, https://doi.org/10.1002/pip.2866.

[22] J.H. Wohlgemuth, S. Kurtz, Reliability testing beyond Qualification as a key component in photovoltaic's progress toward grid parity, in: 2011 Int. Reliab. Phys. Symp., 2011: p. 5E.3.1-5E.3.6. 10.1109/IRPS.2011.5784534.

[23] Y. Zhang, T. Dun, J. Du, X. Liu, H. Li, Q. Dong, T. Liu, Y. Huang, H. Jia, Y. Mai, How double-glass laminated amorphous silicon solar modules break in the field: A case study, in: 2013 IEEE 39th Photovolt, Spec. Conf. PVSC 2013 (2013) 3279–3283, https://doi.org/10.1109/PVSC.2013.6745151.

[24] O.-L. Ouabi, P. Pomarede, N.F. Declercq, N. Zeghidour, M. Geist, C. Pradalier, Learning the propagation properties of rectangular metal plates for Lamb wave-based mapping, Ultrasonics 123 (2022) 106705, https://doi.org/10.1016/j.ultras.2022.106705.

[25] D. Silitonga, N.F. Declercq, P. Pomarède, F. Meraghni, B. Boussert, P. Dubey, Ultrasonic guided waves interaction with cracks in the front glass of thin-film solar photovoltaic module, Sol. Energy Mater. Sol. Cells 251 (2023) 112179, https://doi.org/10.1016/j.solmat.2022.112179.

[26] Y. Wei, K. Tribikram, Guided Waves in multilayered plates for internal defect detection, J. Eng. Mech. 124 (1998) 311–318, https://doi.org/10.1061/(ASCE)0733-9399(1998)124:3(311).

[27] S. Huo, H. Reis, Estimation of adhesive bond strength in laminated safety glass using guided mechanical waves: Part I. An energy velocity approach, Insight Non-Destr. Test. Cond. Monit. 50 (2007), https://doi.org/10.1784/insi.2008.50.3.146.

[28] D.J. Silitonga, N.F. Declercq, Evaluation of laminated glass adhesion strength based on Lamb waves through the observation of the Schoch effect, Acta Acust. 7 (2023) 14, https://doi.org/10.1051/aacus/2023010.

[29] A.R. Clough, R.S. Edwards, Characterisation of hidden defects using the near-field ultrasonic enhancement of Lamb waves, Ultrasonics 59 (2015) 64–71, https://doi.org/10.1016/j.ultras.2015.01.012.

[30] B. Boashash, ed., Chapter I: The Time-Frequency Approach: Essence and Terminology00Author: B. Boashash, Qatar University, Doha, Qatar; University of Queensland Centre for Clinical Research, Brisbane, QLD, Australia (boualem@qu.edu.qa)., in: Time-Freq. Signal Anal. Process. Second Ed., Academic Press, Oxford, 2016: pp. 3–29. 10.1016/B978-0-12-398499-9.09991-X.

[31] S. Lampman, M. Mulherin, R. Shipley, Nondestructive testing in failure analysis, J. Fail. Anal. Prev. 22 (2022) 66–97, https://doi.org/10.1007/s11668-021-01325-1.

[32] M.J.S. Lowe, O. Diligent, Low-frequency reflection characteristics of the s0 Lamb wave from a rectangular notch in a plate, J Acoust Soc Am 111 (2002) 12.

[33] M.J.S. Lowe, P. Cawley, J.-Y. Kao, O. Diligent, The low frequency reflection characteristics of the fundamental antisymmetric Lamb wave a0 from a rectangular notch in a plate, J. Acoust. Soc. Am. 112 (2002) 12.

[34] K.S. Tan, N. Guo, B.S. Wong, C.G. Tui, Experimental evaluation of delaminations in composite plates by the use of Lamb waves, Compos. Sci. Technol. 53 (1995) 77–84, https://doi.org/10.1016/0266-3538(94)00076-X.

[35] N. Toyama, J. Takatsubo, Lamb wave method for quick inspection of impact-induced delamination in composite laminates, Compos. Sci. Technol. 64 (2004) 1293–1300, https://doi.org/10.1016/j.compscitech.2003.10.011.

[36] L. Mallet, B.C. Lee, W.J. Staszewski, F. Scarpa, Structural health monitoring using scanning laser vibrometry: II. Lamb waves for damage detection, Smart Mater. Struct. 13 (2004) 261, https://doi.org/10.1088/0964-1726/13/2/003.
[37] M.A.Y. Barakat, A.-E.-A.-A. El-Wakil, E.H. Hasan, Modification of ultrasonic transducers to study crack propagation in vinyl polymers, supported by SEM technique, J. Vinyl Addit. Technol. 29 (2023) 84–99, https://doi.org/10.1002/vnl.21945.
[38] A.-M. Šimundić, Measures of Diagnostic Accuracy: Basic Definitions, EJIFCC 19 (2009) 203–211.
[39] Paola Galdi, Roberto Tagliaferri, Data Mining: Accuracy and Error Measures for Classification and Prediction, in: Encycl. Bioinforma. Comput. Biol. ABC Bioinforma., Elsevier, 2018.
[40] A. Baratloo, M. Hosseini, A. Negida, G. El Ashal, Part 1: simple definition and calculation of accuracy, sensitivity and specificity, Emergency 3 (2015) 48–49.